



Topological Dirac states in a layered telluride TaPdTe₅ with quasi-one-dimensional PdTe₂ chainsWen-He Jiao ^{1,*}, Xiao-Meng Xie,¹ Yi Liu,² Xiaofeng Xu,² Bin Li,^{3,4} Chun-Qiang Xu,⁵ Ji-Yong Liu,⁶ Wei Zhou,⁷ Yu-Ke Li,⁸ Hai-Yang Yang ⁸, Shan Jiang,⁹ Yongkang Luo,⁹ Zeng-Wei Zhu,⁹ and Guang-Han Cao^{10,11}¹Department of Applied Physics, Zhejiang University of Science and Technology, Hangzhou 310023, China²Department of Applied Physics, Zhejiang University of Technology, Hangzhou 310023, China³New Energy Technology Engineering Laboratory of Jiangsu Province and School of Science, Nanjing University of Posts and Telecommunications, Nanjing 210023, China⁴National Laboratory of Solid State Microstructures, Nanjing University, Nanjing 210093, China⁵School of Physics and Key Laboratory of MEMS of the Ministry of Education, Southeast University, Nanjing 211189, China⁶Department of Chemistry, Zhejiang University, Hangzhou 310027, China⁷Department of Physics, Changshu Institute of Technology, Changshu 215500, China⁸Department of Physics, Hangzhou Normal University, Hangzhou 310036, China⁹Wuhan National High Magnetic Field Center and School of Physics, Huazhong University of Science and Technology, Wuhan 430074, China¹⁰Department of Physics, Zhejiang Province Key Laboratory of Quantum Technology and Devices, Interdisciplinary Center for Quantum Information, and State Key Lab of Silicon Materials, Zhejiang University, Hangzhou 310027, China¹¹Collaborative Innovation Centre of Advanced Microstructures, Nanjing 210093, China

(Received 20 April 2020; accepted 3 August 2020; published 27 August 2020)

We report the synthesis and systematic studies of a new layered ternary telluride TaPdTe₅ with quasi-one-dimensional PdTe₂ chains. This compound crystallizes in a layered orthorhombic structure with space group *Cmcm*. Analysis of its curved field-dependent Hall resistivity, using the two-band model, indicates the hole-dominated transport with a high mobility $\mu_h = 2.38 \times 10^3 \text{ cm}^2 \text{ V}^{-1} \text{ s}^{-1}$ at low temperatures. The in-plane magnetoresistance (MR) displays significant anisotropy with field applied along the crystallographic *b* axis. The MR with the current applied along the *c* axis is also measured in high magnetic fields up to 51.7 T. Remarkably, it follows a power-law dependence and reaches $(9.5 \times 10^3)\%$ at 2.1 K without any signature of saturation. The de Haas–van Alphen oscillations show a small Fermi surface pocket with a nontrivial Berry phase. The Shubnikov–de Haas (SdH) oscillations are detected at low temperatures and under magnetic fields above 28.5 T. Two effective masses m^* ($0.26m_e$ and $0.41m_e$) are extracted from the oscillatory SdH data. Our first-principles calculations unveil a topological Dirac cone in its surface states, and, in particular, the topological index indicates that TaPdTe₅ is a topologically nontrivial material.

DOI: [10.1103/PhysRevB.102.075141](https://doi.org/10.1103/PhysRevB.102.075141)**I. INTRODUCTION**

Topological insulators (TIs) are characterized by robust gapless edge or surface states with a linear Dirac dispersion, which are a direct physical consequence of the nontrivial topology of the bulk band structure and protected by time-reversal symmetry [1,2]. Since the remarkable discovery of TIs, the search for new topological materials has been one of the most interesting topics in condensed matter physics. The classification of materials based on symmetry and topology has been extended to metals, semimetals, and even superconductors. For example, three-dimensional (3D) topological Dirac and Weyl semimetals have conduction and valence bands dispersing linearly through nodal points [3–10]. When these corresponding bands are doubly degenerate, the materials are named Dirac semimetals (DSMs) [4–7]. In the presence of broken time-reversal symmetry or space-inversion symmetry, DSMs evolve into Weyl semimetals (WSMs), and

each Dirac cone in DSMs splits into a pair of Weyl cones with opposite chirality due to the lifted spin degeneracy [8–10]. Lorentz invariance breaking can further give rise to type-II Dirac fermions with a tilted Dirac cone in DSMs [11,12], and type-II Weyl fermions with a tilted Weyl cone in WSMs [13]. If Dirac band crossings take place along a one-dimensional line or loop, in contrast with discrete nodal points in conventional DSMs or WSMs, nodal points turn into the lines of Dirac nodes, which is the band feature of unconventional topological nodal-line semimetals [14,15]. The topological materials usually display exotic properties such as large magnetoresistance (MR) [16], high charge carrier mobility [16,17], chiral anomalies [18,19], exotic superconductivity [20,21], and novel quantum oscillations [22], providing a platform to promote the wide-ranging applications in next-generation spintronics and quantum computing [1,2].

Among the reported topological materials so far, the transition-metal tellurides take up a large proportionality. For instance, the binary tellurides Bi₂Te₃ [23,24] and Sb₂Te₃ [23] were proposed and evidenced to be TIs. (W, Mo)Te₂ [25,26] and *TM*Te₂ (*TM* = Pd, Pt, Ni) [27–29] were confirmed to

*Corresponding author: whjiao@zust.edu.cn

host type-II Weyl and type-II Dirac fermions, respectively. Very recently, the ternary tellurides $MTMTe_4$ ($M = \text{Nb, Ta}$; $TM = \text{Ir, Rh}$) were theoretically predicted as a new series of type-II WSMs, and expected to host a minimum of four Weyl points within the first Brillouin zone by including spin-orbit coupling (SOC) [30,31]. Experimental results verify the existence of Weyl points in TaIrTe_4 and NbIrTe_4 [32–34]. Unconventional surface superconductivity, exhibiting quasi-one-dimensional (quasi-1D) and topologically nontrivial characteristics, was even observed in TaIrTe_4 [35]. From a crystal-structure viewpoint, both TaIrTe_4 and NbIrTe_4 have a layered crystal structure, the two-dimensional (2D) atomic layer of which is composed of alternating quasi-1D IrTe_2 and $(\text{Ta, Nb})\text{Te}_2$ chains. This structural feature is very common among ternary transition-metal tellurides, reminiscent of the ternary Pd-based tellurides $\text{Ta}_4\text{Pd}_3\text{Te}_{16}$ and $\text{Ta}_3\text{Pd}_3\text{Te}_{14}$, in both of which we reported superconductivity recently [36,37]. The structural similarity and exotic properties found among ternary transition-metal tellurides motivate us to further explore novel topological materials and even long-sought-after topological superconductors in these low-dimensional systems.

While a large number of materials have hitherto been identified to be topologically nontrivial, most of them are 2D or 3D electronically, and the quasi-1D analogs are extremely rare [32,33,38]. In quasi-1D materials, the competing ground states, such as charge/spin density waves or even superconductivity, often prevail and therefore elude the experimental detection of the topological carriers. Here, we report synthesis and characterizations of a new ternary Pd-based telluride TaPdTe_5 , which explicitly shows a layered crystal structure with quasi-1D characteristics. Interestingly, the Shubnikov–de Haas (SdH) oscillations of the resistivity under high magnetic fields up to 51.7 T give the light effective masses of charge carriers. Our experiments also reveal a large unsaturated MR on the order of $\sim 10^4\%$ along with large anisotropy. From the analyses of de Haas–van Alphen (dHvA) oscillations, we have seen typical signatures of Dirac fermions in TaPdTe_5 . The first-principles calculations further reveal topologically nontrivial states therein. Our results suggest the new material TaPdTe_5 hosts a topological nontrivial Berry phase and thus provides another platform to investigate topological physics in ternary transition-metal tellurides.

II. EXPERIMENTAL METHODS

A. Sample synthesis

Single crystals of TaPdTe_5 were grown using a self-flux method, similar to that in growing $\text{Ta}_4\text{Pd}_3\text{Te}_{16}$ and $\text{Ta}_3\text{Pd}_3\text{Te}_{14}$ single crystals [36,37], but the growth parameters were varied. The early attempt to synthesize TaPdTe_5 failed but made $\text{Ta}_3\text{Pd}_3\text{Te}_{14}$ accidentally prepared [39]. Powders of the elements Ta (99.97%), Pd (99.995%), and Te (99.99%) used as reagents, in an atomic ratio of $\text{Ta} : \text{Pd} : \text{Te} = 2 : 5 : 25$, were thoroughly mixed together, loaded, and sealed into an evacuated quartz ampule. All the procedures handling the reagents were done in a glove box filled with highly pure argon gas. The ampule was slowly heated up to 1223 K and held for 24 h. After that, it was cooled to 923 K at a rate of

5 K/h, then followed by cooling down to room temperature. Large shiny gray-black flattened needle-like crystals with the dimensions up to $2 \times 0.4 \times 0.1 \text{ mm}^3$ were harvested [see the left inset of Fig. 1(a)]. The air-stable crystals are malleable, and can be easily exfoliated to a thin layer by a razor blade.

B. Structure and composition determination

The chemical composition of the as-grown single crystals was measured by energy-dispersive x-ray spectroscopy (EDS) with an AMETEK©EDAX (Model Octane Plus) spectrometer, equipped in a field-emission scanning electron microscope (Hitachi S-4800). Figure 1(b) shows the typical EDS spectrum for a piece of crystal. The average chemical composition of the as-grown crystals is determined to be $\text{Ta}_{1.00}\text{Pd}_{0.95}\text{Te}_{5.91}$. The obtained concentration of Te tends to be larger than the actual one, possibly due to some systematic errors in the calculation process.

X-ray diffraction (XRD) data collection from this single crystal was performed on an Xcalibur, Atlas, Gemini Ultra diffractometer. The crystal was mounted on the CCD goniometer head, followed by diffraction data collections at room temperature. Data collection, integration, and absorption correction were done in the X-area software package. The structure of TaPdTe_5 was solved by a direct method and refined by full-matrix least squares based on F^2 using a SHELXTL program package [40]. The results indicate TaPdTe_5 adopts a C -centered orthorhombic structure with a space group $Cmcm$ (No. 63), which respects inversion symmetry. Atomic coordinates and thermal displacement parameters (U_{eq}) are given in Tables S1 and S2 of the Supplemental Material (SM) [41]. The related bond lengths and bond angles are given in Table S3 of the SM. Single-crystal XRD data collection was also performed at room temperature with a monochromatic $\text{Cu } K_{\alpha 1}$ radiation using a PANalytical x-ray diffractometer (model EMPYREAN) radiation by a conventional θ - 2θ scan for a crystal lying on a sample holder. As shown in Fig. 1(a), only multiple peaks arising from the diffraction from (010) planes can be observed, consistent with the layered crystal structure of TaPdTe_5 . The interplane spacing is determined to be 6.628 Å by this XRD, and this value is very close to half of the lattice parameter b ($b/2 = 6.637$ Å) tabulated in Table I. The layered nature of its structure is similar to that of the other two ternary Pd-based tellurides, $\text{Ta}_4\text{Pd}_3\text{Te}_{16}$ and $\text{Ta}_3\text{Pd}_3\text{Te}_{14}$ [36,37]. To exhibit the obvious difference of the interlayer spacing among them, we plot the fourth reflection of XRD patterns together for TaPdTe_5 , $\text{Ta}_4\text{Pd}_3\text{Te}_{16}$, and $\text{Ta}_3\text{Pd}_3\text{Te}_{14}$, namely (080), (-4012) , and (-808) , respectively, in the right inset of Fig. 1(a). By this means, one can easily distinguish the TaPdTe_5 crystal from the other two, even though all these three crystals are of the same shiny gray-black striplike exterior.

C. Physical property measurements

The resistivity and low-field magnetoresistivity measurements were carried out in a physical property measurement system (PPMS-9, Quantum Design) with ac transport option (typical excitation current 1 mA). A standard four-probe method was employed for the resistivity measurements. The

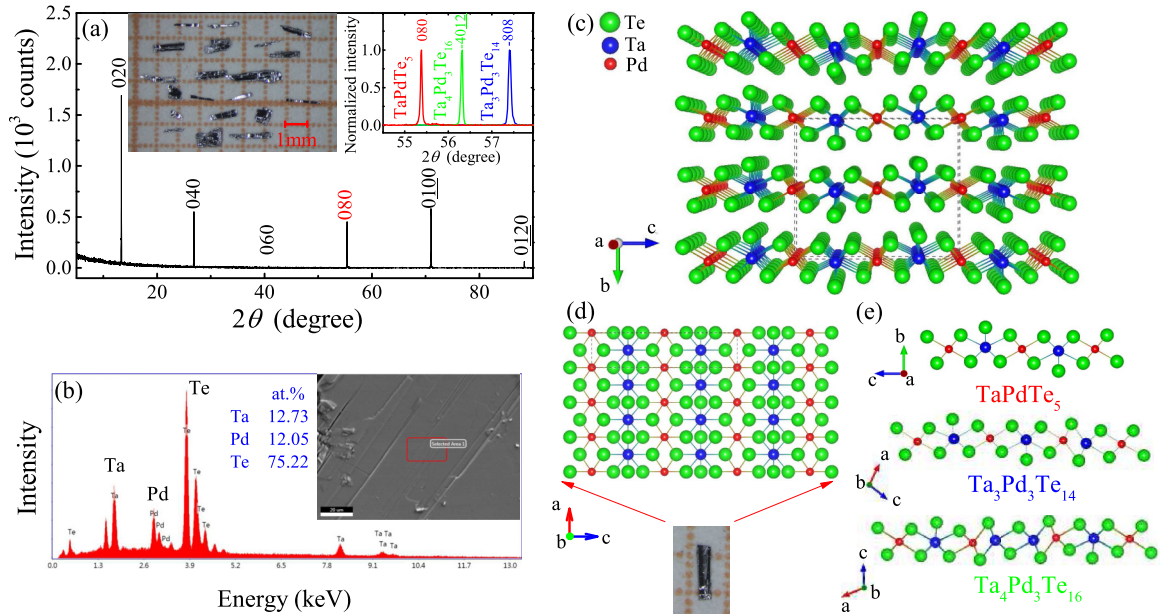


FIG. 1. Sample characterizations and crystallographic structure of TaPdTe₅. (a) Single-crystal x-ray diffraction pattern. The left inset is a photograph of the TaPdTe₅ crystals on a millimeter-grid paper. The right inset shows the fourth reflection in x-ray diffraction pattern for TaPdTe₅, Ta₄Pd₃Te₁₆, and Ta₃Pd₃Te₁₄, respectively. (b) A typical energy-dispersive x-ray spectrum with electron beams focused on the selected area (marked in the inset) of the crystals. (c) Crystal structure of TaPdTe₅ viewed perspectively along the *a* axis. (d) An individual atomic layer of TaPdTe₅ projected along the *b* axis. The lower panel of (d) is a piece of the flattened needle-like crystal under an optical microscope, from which the layered and needle-like morphology can be clearly identified. (e) Projection view of one atomic layer of TaPdTe₅ (upper), Ta₃Pd₃Te₁₄ (middle), and Ta₄Pd₃Te₁₆ (bottom) along the chain direction.

Hall effect measurement was performed by reversing the field direction and antisymmetrizing the data. Eight pieces of crystals with a total mass of 2.4 mg were used for the specific heat measurement on the PPMS. High-field MR data up to 51.7 T were obtained from pulsed high magnetic field equipment at Wuhan National High Magnetic Field Center. Magnetic susceptibility measurements were performed on a commercial Quantum Design magnetic property measurement system (MPMS-7).

D. Band structure calculations

We carried out first-principles calculations for band structure based on our experimental crystal structure. The electronic structure calculations with high accuracy were performed using the full-potential linearized augmented plane wave (FP-LAPW) method implemented in the WIEN2k code [42]. The generalized gradient approximation (GGA) presented by Wu and Cohen [43] was applied to the exchange-correlation potential calculation. The muffin tin radii were chosen to be 2.5 a.u. for all atoms. The plane-wave cutoff was defined by $RK_{\max} = 7.0$, where R is the minimum LAPW sphere radius and K_{\max} is the plane-wave vector cutoff. To calculate the surface electronic structure, we constructed a first-principles tight-binding model Hamiltonian, where the tight-binding model matrix elements were calculated by projecting onto the Wannier orbitals [44]. We used Ta *d*, Pd *d*, and Te *p* orbitals to construct Wannier functions. The surface state spectrum of the (001) slab was calculated with the surface Green's function methods as implemented in

WannierTools [45]. Relativistic effects and SOC were included in the calculations.

III. RESULTS AND DISCUSSION

The layered structure of TaPdTe₅ is displayed in Fig. 1(c), which shows the eclipsed stacking of the layers along the *b* axis. The layered slab, as shown in Fig. 1(d), is composed of two alternating unique chains that run parallel to the *a* axis. The chains are face-sharing Ta bicapped trigonal prisms and edge-sharing Pd octahedra. The types of coordination are common for the tellurides, such as two other ternary Pd-based tellurides Ta₄Pd₃Te₁₆ and Ta₃Pd₃Te₁₄. To compare the different constitution of the layered slab, we plot in Fig. 1(e) the atomic layer of the three tellurides. It is interesting to note that we recently reported the superconductivity in both Ta₄Pd₃Te₁₆ and Ta₃Pd₃Te₁₄ [36,37]. TaPdTe₅ is isostructural with NbNiTe₅ [46] and Ta*TM*Te₅ (*TM* = Ni, Pt) [39,47], for all of which the chains of transition metal atoms in one layer are aligned with the chains of transition metal atoms in adjacent layers in the *b* direction. The same is true of the Ta or Nb chains. The other layered telluride NbPdTe₅, which has the same stoichiometry and almost identical atomic layer, is of a different structure type (*Pnma*), because of the different ordering of the layers being staggered rather than eclipsed [48]. Due to the similar atomic radius, Nb and Ta usually have similar coordination preferences in tellurides. It is therefore rare that the substitution of Nb for Ta in NbPdTe₅ yields TaPdTe₅ with a despite similar but different structure.

The electrical resistivity, measured with the current applied along the *a* [Fig. 2(a)], *c* [Fig. 2(b)], and *b* [Fig. 2(c)]

TABLE I. Crystallographic data and experiment details for TaPdTe₅.

Parameter	Value
T of data collection (K)	296.02
Wavelength (Å)	0.71073
Formula weight (g mol ⁻¹)	925.37
Crystal system	orthorhombic
Space group	<i>Cmcm</i>
a (Å)	3.6934(4)
b (Å)	13.2740(13)
c (Å)	15.6020(15)
Volume (Å ³)	764.91(13)
Z	4
Density (calculated) (g cm ⁻³)	8.04
μ (mm ⁻¹)	35.225
$F(000)$	1516
Crystal size (mm ³)	0.23 × 0.12 × 0.05
θ range for data collection (deg)	2.611 to 26.475
Index ranges	-4 ≤ h ≤ 4 -16 ≤ k ≤ 16 -19 ≤ l ≤ 19
Reflection collected	3574
Independent reflections	479 ($R_{\text{int}} = 0.0577$)
Completeness to $\theta = 25.242^\circ$	99.8%
Data/restraints/parameters	479/0/25
Goodness of fit	1.107
Final R indices ^a [$>2\sigma(I)$]	$R_{\text{obs}} = 0.0474$ $\omega R_{\text{obs}} = 0.1506$
R indices (all data)	$R_{\text{all}} = 0.0486$ $\omega R_{\text{all}} = 0.1526$

$$^a R = \frac{\sum ||F_o| - |F_c||}{\sum |F_o|}, \quad \omega R = \left\{ \frac{\sum [(\omega(|F_o|^2 - |F_c|^2)^2)]}{\sum [\omega(|F_o|^4)]} \right\}^{1/2},$$

$$\text{and } \omega = 1/[\sigma^2(F_o^2) + (0.1162P)^2 + (22.3597P)], \quad \text{where } P = (F_o^2 + 2F_c^2)/3.$$

directions, shows metallic behavior from room temperature to 2 K with a residual resistivity ratio $\text{RRR} = \rho_a(300\text{ K})/\rho_a(2\text{ K}) = 59$. No indication of superconducting transition can be observed down to 0.5 K measured in a ³He cryostat (data not shown here). The room-temperature resistivity $\rho_a(300\text{ K})$ has a value of $\sim 33\ \mu\Omega\text{ cm}$, indicating a high degree of metallicity. From room temperature down to 50 K, $\rho_a(T)$, $\rho_c(T)$, and $\rho_b(T)$ follow an approximately linear temperature (T) dependence. Below 50 K, however, all of them cross over to a quadratic T dependence, i.e., $\rho(T) = \rho_0 + AT^2$, a Fermi liquid behavior, indicating the electron-electron scattering dominates in the low-temperature region. The T dependence of resistivity anisotropy ρ_c/ρ_a and ρ_b/ρ_a is plotted in Fig. 2(d). The quasi-1D transport behaviors are clearly exhibited with $\rho_a : \rho_b : \rho_c = 1 : 24.9 : 4.3$ at 300 K, and $1 : 252.1 : 4$ at 2 K. The small value of ρ_c/ρ_a suggests a weak anisotropy in the layered slab, comparable with that of the superconductor Ta₄Pd₃Te₁₆ [49]. The most striking feature of the data is the sharp increase of the anisotropy for ρ_b/ρ_a around 60 K, making the value at 2 K almost 1 order of magnitude larger than that at 300 K. A broad maximum also appears around 60 K for ρ_c/ρ_a . The origin of this anomaly is unclear at this stage. The magnetic susceptibility of TaPdTe₅ measured at a magnetic field of 1 T

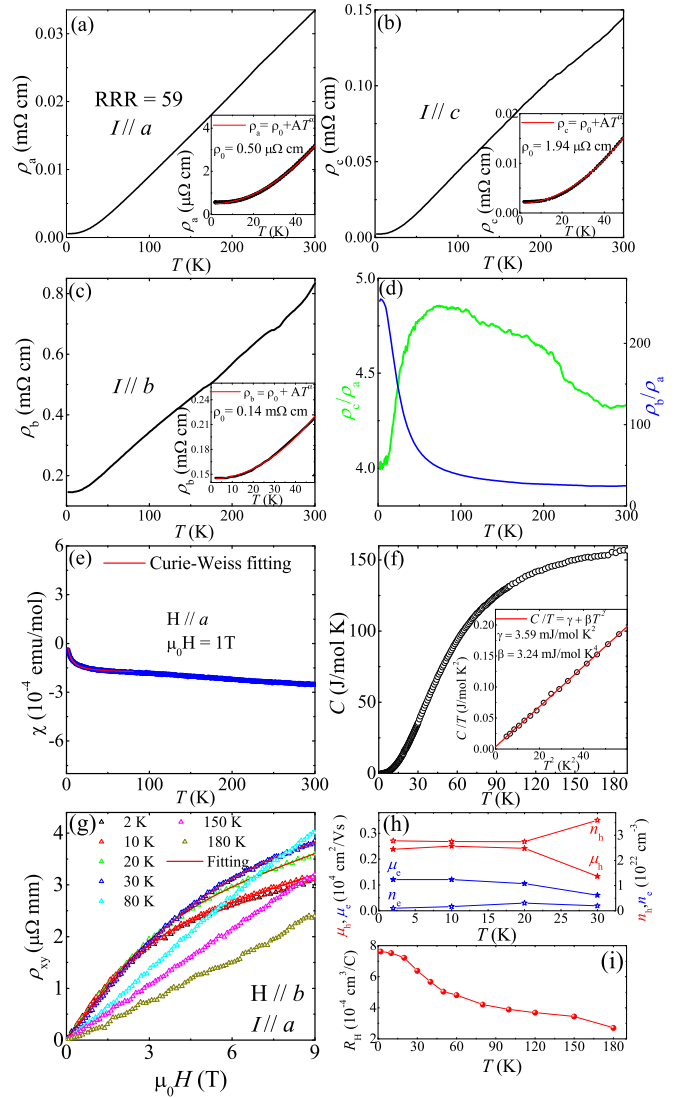


FIG. 2. Physical properties of TaPdTe₅. (a), (b), (c) Temperature dependence of the electronic resistivity ρ_a , ρ_c , and ρ_b with the current applied along the a axis (a), c axis (b), and b axis (c), respectively. The insets of (a), (b), and (c) are an enlarged view of $\rho(T)$ in the low-temperature regime and the fit to $\rho(T) = \rho_0 + AT^2$. (d) Temperature dependence of the resistivity anisotropy for ρ_c/ρ_a and ρ_b/ρ_a . (e) Temperature dependence of the magnetic susceptibility $\chi(T)$, measured at the 1 T field parallel to the chain direction. (f) The heat capacity at zero field below 185 K. The inset separates the electronic and phononic contributions. (g) The Hall resistivity at different temperatures below 180 K. The red dashed lines are fits based on a two-band model. (h) Temperature dependence of the carrier density n and the mobility μ extracted from the above fits. (i) The temperature dependence of low-field Hall coefficients extracted by linear fitting.

is shown in Fig. 2(c). It is apparent that $\chi(T)$ is almost T independent in the high-temperature range. Below $T \sim 20\text{ K}$, the magnetization undergoes a slight increase. $\chi(T)$ from 2 K to 80 K can be well described by the Curie-Weiss expression $\chi(T) = \chi_0 + \frac{C}{T - \theta}$, where χ_0 is the temperature-independent contribution, C is the Curie constant, and θ is the Curie-Weiss temperature. The fit gives $\chi_0 = -1.82(1) \times 10^{-4}\text{ emu/mol}$,

$C = 8.17(4) \times 10^{-4}$ emu K/mol, and $\theta = 3.48(6)$ K. An effective moment calculated by the formula $\mu_{\text{eff}} = (8C)^{1/2}$ gives $0.0809(1) \mu_B$. Such a small μ_{eff} , corresponding to $\sim 4.68\%$ of that for an unpaired electron, indicates the Curie-Weiss contribution is most likely from tiny magnetic impurities. Therefore, TaPdTe₅ is expected to be paramagnetic, similar to TaPtTe₅ and NbPdTe₅ [47]. By subtracting the Curie-Weiss-like contribution, we estimate the T -independent magnetic susceptibility as $\chi_0 = \chi_p + \chi_{\text{vv}} + \chi_L + \chi_{\text{core}} = -1.82(1) \times 10^{-4}$ emu/mol, which includes a Pauli paramagnetism (χ_p), van Vleck paramagnetism (χ_{vv}), Landau diamagnetic susceptibility (χ_L), and core diamagnetism (χ_{core}). The χ_L is estimated to be $\sim -\frac{1}{3}\chi_p$ by assuming χ_L being not enhanced by the electron-phonon interaction. χ_{core} is calculated to be $-2.25(5) \times 10^{-4}$ emu/mol from those of constituent ions in Ref. [50]. The upper limit of the Pauli paramagnetic susceptibility is then estimated to $\chi_p = 0.546 \times 10^{-4}$ emu/mol by neglecting χ_{vv} . The density of states at Fermi energy level $N(E_F)$ could be derived to be $1.69 \text{ eV}^{-1} \text{ fu}^{-1}$ from the formula $N(E_F) = \frac{\chi_p}{\mu_0 \mu_B}$, where μ_0 and μ_B denote the vacuum permeability and Bohr magneton, respectively. We can also obtain the Sommerfeld parameter $\gamma_n = 3.99 \text{ mJ mol}^{-1} \text{ K}^{-2}$ by the relation $\gamma_n = k_B^2 \pi^2 N(E_F)/3$ for noninteracting electron systems, where k_B is the Boltzmann constant.

The T -dependent specific heat, as shown in Fig. 2(d), shows no evident anomaly below 190 K. The data below 8 K can be well described by the equation $C = \gamma T + \beta T^3$ shown in the inset of Fig. 2(d), where γT represents the electron contribution and βT^3 represents the phonon contribution. The fit yields $\gamma = 3.59 \text{ mJ mol}^{-1} \text{ K}^{-2}$, close to the upper limit of γ_n as analyzed above, and $\beta = 3.24 \text{ mJ mol}^{-1} \text{ K}^{-4}$, from which the Debye temperature Θ_D is estimated to be 161.39 K. The Wilson ration $R_W (= \pi^2 k_B^2 \chi_p / 3 \mu_0 \mu_B^2 \gamma)$ can measure the relative enhancements of the spin susceptibility and electronic specific heat [51]. To estimate the strength of the electron-electron correlation effect, we calculate the Wilson ratio as ~ 1.1 , very close to the value ($R_W = 1$) of a noninteracting Fermi liquid. This suggests that the electron-electron correlation effect is negligible in TaPdTe₅.

The Hall resistivity ρ_{xy} up to 9 T at selected temperatures below 180 K is shown in Fig. 2(e), from which nonlinear field-dependent ρ_{xy} can be clearly observed, reflecting the multiband characteristic in TaPdTe₅. The positive value of ρ_{xy} indicates the dominance of hole-type charge carriers. We apply a simplified two-carrier model including one electron-type band and one hole-type band, in an effort to extract the charge carrier densities and mobilities. According to the classical expression for the Hall coefficient, including both electron- and hole-type carriers [52],

$$\frac{\rho_{xy}}{\mu_0 H} = \frac{1}{e} \frac{(\mu_h^2 n_h - \mu_e^2 n_e) + (\mu_h \mu_e)^2 (\mu_0 H)^2 (n_h - n_e)}{(\mu_e n_h + \mu_h n_e)^2 + (\mu_h \mu_e)^2 (\mu_0 H)^2 (n_h - n_e)^2}, \quad (1)$$

where e is the absolute value of electronic charge, and $n_{e(h)}$ and $\mu_{e(h)}$ are the carrier densities and mobilities of the electrons (holes), respectively. This equation predicts immediately a nonlinear field dependence, once two carrier types are present. The fit is well performed by the nonlinear

data below 30 K. It is apparent that the hole density n_h ($2.78 \times 10^{22} \text{ cm}^{-3}$ at 2 K) is much higher than the electron density n_e ($9.43 \times 10^{20} \text{ cm}^{-3}$ at 2 K). Moreover, the holes have much higher mobility ($2.38 \times 10^3 \text{ cm}^2 \text{ V}^{-1} \text{ s}^{-1}$ at 2 K) than the electrons ($1.21 \times 10^3 \text{ cm}^2 \text{ V}^{-1} \text{ s}^{-1}$ at 2 K). Both $n_{e(h)}$ and $\mu_{e(h)}$ vary not too much within this temperature interval. At high temperatures ($T > 30$ K), ρ_{xy} is still positive and develops linearly with the field, indicating the single hole-type carriers dominate the transport. Clearly, this result excludes the possibility of electron-hole compensation effect in TaPdTe₅. The T -dependent Hall coefficient R_H is plotted in Fig. 2(f), obtained by linear fitting with the ρ_{xy} below the field 1.5 T. The obvious T -dependent $R_H(T)$ is also signaling multiple bands with coexisting hole and electron pockets, consistent with the above analysis, as each band can have a distinct T -dependent mobility.

The MR of ρ_a under magnetic field \mathbf{H} parallel to the b direction up to 9 T is shown in Fig. 3(a), from which we can see that the T evolutions of ρ_a under different fields are almost identical. We also measured the field-dependent MR of ρ_a at several fixed temperatures, defined as $\Delta\rho_a/\rho_a(0 \text{ T})$ [$\Delta\rho_a = \rho_a - \rho_a(0 \text{ T})$]. As noticed in Fig. 3(c), the MR of ρ_a is weak, reaching only 87% at 2 K and 9 T. Importantly, its field dependence is quite linear at low temperatures, a feature seen in many topological materials due to the distinct spectrum of Landau levels for Dirac fermions in the field [16,53], while a seemingly quadratic contribution can be observed in low field. For a standard metal with the presence of both electrons and holes, a quadratic T dependence is expected at low field and the MR tends to saturate at high field; i.e., MR should scale as $\frac{\alpha(\mu_0 H)^2}{\beta + (\mu_0 H)^2}$ [54]. Hence, the overall MR data with both Dirac fermions and conventional carriers can be fitted by a linear term in addition to a conventional component, i.e., $\frac{\Delta\rho_a}{\rho_a} = \frac{\alpha(\mu_0 H)^2}{\beta + (\mu_0 H)^2} + \gamma \mu_0 H$. As shown in Fig. 3(c), the experimental data at 2 K can be fitted very well. The MR of ρ_c under $\mathbf{H} \parallel b$ is rather large, reaching as high as 910% at 2 K and 9 T, nearly 11 times that of ρ_a , as clearly illustrated in Fig. 3(c). The MR of ρ_c can be fitted to a single power law $\Delta\rho_c(\mu_0 H) \propto H^\alpha$ with $\alpha = 1.50$. More interestingly, with increasing the field above 5 T, the T evolution of ρ_c no longer follows the zero-field curve, as shown in Fig. 3(b). Below a ‘‘turn on’’ temperature T^* , defined as the temperature at which the minimum in the resistivity is located, ρ_c begins to increase and finally saturate to a plateau at low temperatures. Very similar resistivity plateaus have been observed in a number of topological semimetals, and have been attributed by some groups to the presence of the topological surface states after excluding the possibility of a magnetic-field-driven metal-insulator transition [55,56]. The ‘‘turn on’’ temperature is linearly shifted to higher temperature as larger fields are applied at the rate of $\sim 2.0 \text{ K T}^{-1}$, as shown in the inset of Fig. 3(b), suggesting competition between dominating scattering mechanisms. The linear dependence of T^* on magnetic fields is also reported in topological material WTe₂ [25]. On the other hand, the MR of many metals and semimetals obeys a general function, commonly referred to as Kohler’s rule, $\Delta\rho/\rho_0 = f(H/\rho_0)$, where ρ_0 is the zero-field resistivity. As shown in Fig. 3(e) and Fig. 3(f), the MR curves of both ρ_a and ρ_c can basically be scaled into a single curve, indicating that Kohler’s rule is

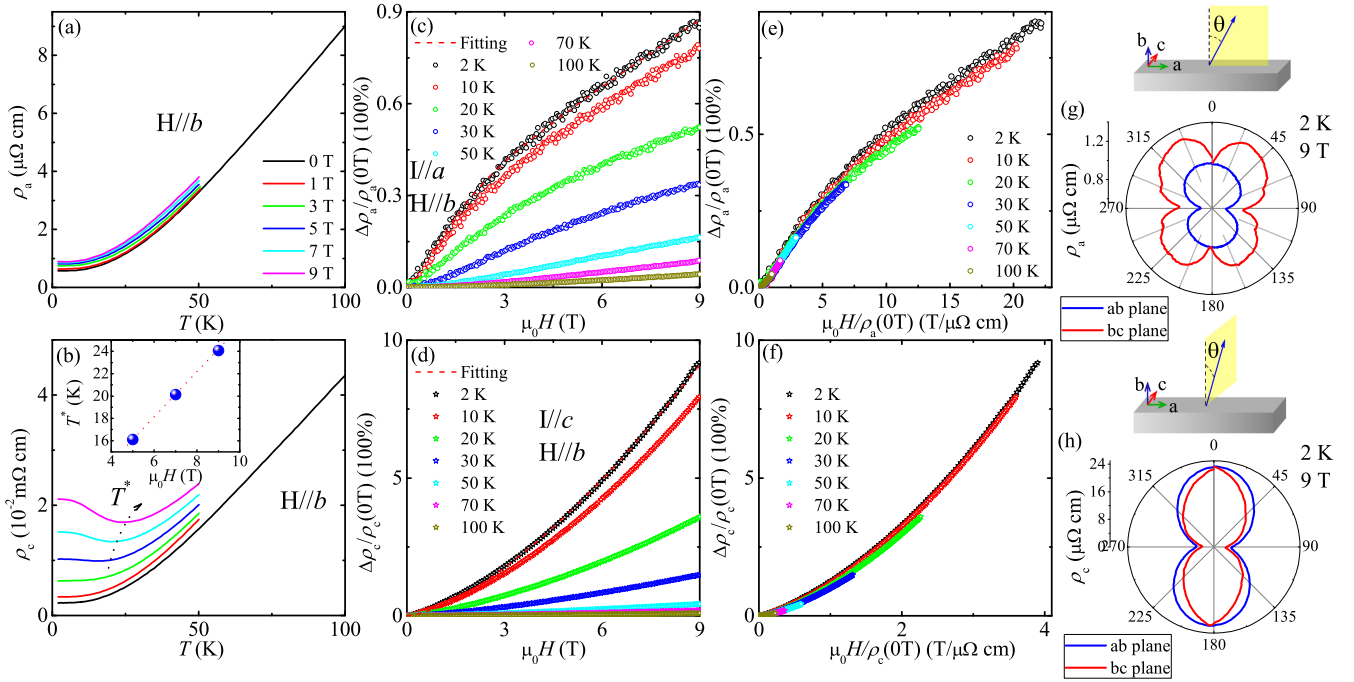


FIG. 3. Temperature dependence of ρ_a (a) and ρ_c (b) with the magnetic fields parallel to the b axis up to 9 T below 50 K. The inset of (b) is the field dependence of T^* . The MR for ρ_a (c) and ρ_c (d) at selected temperatures. The red dashed lines are the fits (see main text). Kohler's scaling for ρ_a (e) and ρ_c (f). Angular dependence of MR at 2 K for ρ_a (g) and ρ_c (h) with magnetic field 9 T being rotated within the ab (blue) and bc (red) planes. The inset shows the definition of field orientation angle θ .

well obeyed over a large temperature range. The validation of Kohler's rule indicates that the upturns and low-temperature plateau of the MR do not reflect an intrinsic field-induced metal-insulator transition, but are rather a consequence of the small residual resistivity and correspondingly high mobilities of the charge carriers [57].

The anisotropic behavior in the MR can be visualized in the angular dependence of magnetoresistivity (AMR). The AMR of ρ_a at 2 K and 9 T is plotted in Fig. 3(g). For fields rotating within the bc plane, $\rho_a(\theta)$ reaches its maximum for $\theta \approx 45^\circ$ and its minimum for $\theta = 0^\circ$ and 90° , resulting in a fourfold-symmetric “butterfly” shaped angular dependence. This butterfly shaped MR was also observed in a few of materials including high- T_c superconductor and topological semimetals, for example, type-II Weyl semimetal NbIrTe₄ [33] and Dirac nodal line semimetal ZrSiS [58]. The unconventional fourfold anisotropy is believed to be governed by the topography of Fermi surface and related anisotropy in effective masses in NbIrTe₄ [33]. In the case of ZrSiS, this behavior is ascribed to a topological phase transition as a function of field orientation that is inherent to the nodal Dirac line [58]. For fields rotating within the ab plane, the AMR data of ρ_a exhibit a typical twofold symmetric “dumbbell” shaped anisotropy, which is expected for a material with 2D or quasi-2D electronic structure and classical Lorentz-type MR, i.e., $\text{AMR} \propto (H \cos \theta)^2$. The possible presence of 2D-like Fermi surface is in line with the layered crystal structure of TaPdTe₅. The AMR of ρ_c at 2 K and 9 T, for fields rotating either within the ab plane or within the bc plane, also shows a “dumbbell” shape with twofold symmetry, as noticed in Fig. 3(h). The AMR at a fixed angle within the ab plane is a little larger than that within the bc plane, resulting in a fatter dumbbell.

To check whether there is any SdH quantum oscillation in TaPdTe₅, we measured the MR under the high magnetic field $\mathbf{H} \parallel b$ up to 51.7 T. The resistivity signal measured with the current along the a axis is indistinguishable. It seems that the resistivity signal is submerged by noisy signal, possibly due to the resistivity R_a being quite small. The MR with the current along the c axis is shown in Fig. 4(a), from which SdH oscillations can be identified above 28.5 T. To extract their amplitude of the oscillations, a third-order polynomial background is subtracted from the resistivity. The resulting oscillations at different temperatures are plotted against the inverse magnetic field, as seen in the upper inset of Fig. 4(a). Applying a fast Fourier transform (FFT), we obtained the corresponding frequency spectra, as plotted in Fig. 4(b). Although the data are not smooth enough, two major frequencies 150 T and 870 T, which are denoted as F_1 and F_2 , respectively, can be clearly identified. The observed frequencies are related to the extremal cross sections of the Fermi surface (A_F) described by the Onsager relation, $F_i = A_i \hbar / (2\pi e)$, where \hbar is the reduced Planck constant. The calculated A_i are $A_1 = 1.43 \text{ nm}^{-2}$ and $A_2 = 8.29 \text{ nm}^{-2}$. The T dependence of the FFT amplitudes of two corresponding frequencies is shown in the inset of Fig. 4(b). The cyclotron effective mass of a given electronic orbit can be extracted from the temperature damping factor R_T in the Lifshitz-Kosevitch (LK) formula and is given by $R_T = \frac{\lambda T}{\sinh(\lambda T)}$ where $\lambda = 2\pi^2 k_B m^* / \hbar e \mu_0 H$, with m^* being the cyclotron effective mass and k_B being the Boltzmann constant. The resultant m^* are $(0.26 \pm 0.01)m_e$ and $(0.41 \pm 0.03)m_e$ for F_1 and F_2 , respectively, where m_e is the free electron mass. The lower inset of Fig. 4(a) shows the MR of R_c . The high-field MR at 2.1 K can be fitted to a power law where $\Delta R_c \propto H^\alpha$ with $\alpha = 1.31$, close to the derived value 1.50

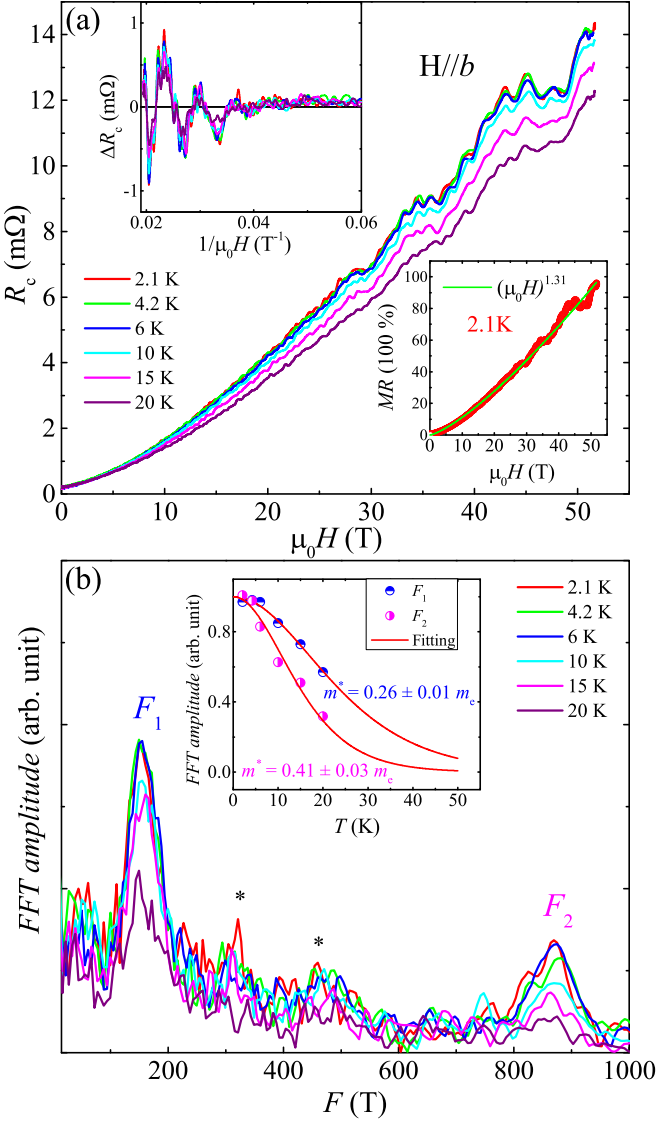


FIG. 4. (a) The high-field MR for ρ_c under $\mathbf{H} \parallel b$ at different temperatures starting from 2.1 K to 20 K. The upper inset shows SdH quantum oscillation after background subtraction. The lower inset shows the normalized MR at 2.1 K. (b) Corresponding FFT amplitudes of SdH oscillations depicting fundamental frequencies F_1 (150 T) and F_2 (870 T). Two small peaks are marked by the asterisk. The inset shows T -dependent FFT amplitudes of F_1 (150 T) and F_2 (870 T) along with their fittings according to Lifshitz-Kosevich relation to obtain their corresponding effective masses.

from fitting the low-field MR. This indicates that the field dependence of MR basically holds in the high-field range. Moreover, the MR does not show any sign of saturation and reaches a magnitude of $(9.5 \times 10^3)\%$ at 51.7 T. In a classical picture, the large nonsaturating transverse MR is due to the vicinity to a perfect balance between electron and hole carriers [25]. Our analysis of the data from Hall effect measurement excludes the electron-hole compensation explanation for the nonsaturating MR, making us conjecture that it might bear relation to the existence of unconventional quasiparticles in TaPdTe₅.

While SdH oscillations can only be observed in the high-field MR when $\mu_0 H$ exceeds 28.5 T, the dHvA effect, the quantum oscillations in magnetic susceptibility, to be discussed below, appear in a magnetic field as low as 1.7 T at 2 K. This inconsistency of SdH and dHvA oscillations is often observed in low-dimensional materials due to the distinct mechanisms of SdH and dHvA oscillations [29]. The isothermal magnetization for $\mathbf{H} \parallel a$ at several temperatures below 20 K shows beautiful quantum oscillations [Fig. 5(a)]. We present the oscillatory components of magnetization, obtained after subtracting the background, in Fig. 5(b). Very strong oscillations are clearly seen. From the FFT analyses, we derive a single frequency of 37 T from the dHvA oscillations for $\mathbf{H} \parallel a$, as shown in Fig. 5(c). The Fermi area (A_F) that is covered by electrons or holes is found to be 0.352 nm^{-2} from the Onsager relation. In general, the oscillatory dHvA data can be described by the standard LK formula [59], with the Berry phase being taken into account [60]:

$$\Delta M \propto -R_T R_D R_S \sin \left[2\pi \left(\frac{F}{\mu_0 H} + \frac{1}{2} - \frac{\varphi_B}{2\pi} - \delta \right) \right], \quad (2)$$

where φ_B is the Berry phase, δ is an additional phase shift determined by the dimensionality of the Fermi surface, R_T , R_D , and R_S are the thermal damping factor, Dingle damping term, and a spin-related damping term, respectively. $R_T = \frac{2\pi^2 k_B m^* T / \hbar e \mu_0 H}{\sinh(2\pi^2 k_B m^* T / \hbar e \mu_0 H)}$, $R_D = \exp(-2\pi^2 k_B T_D m^* / \hbar e \mu_0 H)$, and $R_S = \cos(\pi g m^* / 2m_e)$, where T_D is the Dingle temperature. The oscillation of ΔM is described by the sine term with the phase factor $\frac{1}{2} - \frac{\varphi_B}{2\pi} - \delta$. The phase shift δ is equal to 0 and $\pm 1/8$ (− for electronlike and + for the holelike), respectively, for the 2D and 3D Fermi surfaces. As we have done above, the effective mass m^* can be obtained through the fit of the T dependence of the oscillation amplitude to the thermal damping factor R_T from the LK formula. The effective mass is extracted to be $0.12m_e$, as shown in Fig. 5(d). Using the fitted effective mass as a known parameter, we can further fit the oscillation pattern at 2 K, represented by the black line in Fig. 5(e), to the LK formula, from which quantum mobility and the Berry phase can be extracted. It is well known that the Berry phase is zero for a parabolic energy dispersion and π for a linear energy dispersion. Given that the Fermi surface of TaPdTe₅ is of 2D and/or 3D character, we adopt both all possible values of δ . The fit gives the Berry phase as 1.24π , 1.49π , and 0.99π for $\delta = 0$, $-1/8$, and $1/8$, respectively. The fitted Dingle temperature T_D is 5.85 K, corresponding to the quantum relaxation time $\tau_q = \hbar / (2\pi k_B T_D) = 2.08 \times 10^{-13} \text{ s}$ and quantum mobility $\mu_q = e\tau / m^* = 3159 \text{ cm}^2 \text{ V}^{-1} \text{ s}^{-1}$. The Berry phase can also be extracted from the Landau fan diagram as shown in Fig. 5(f) [15]. The valley in the magnetization should be assigned with a Landau level (LL) index of $n - 1/4$. The red line in Fig. 5(f) is the linear fit of the LL indices. The slope of the linear fit is 36.8 T, in good agreement with the frequency obtained from the FFT analysis. The inset of Fig. 5(f) is an enlarged view near $1/\mu_0 H \rightarrow 0$. The intercept at the n abscissa from the linear fit is 0.39 ± 0.03 , corresponding to a nontrivial Berry phase of $\varphi_B = 2\pi|0.39 + \delta|$. A nearly 1/2-shift possibly distinguishes the Dirac spectrum from the Schrödinger case

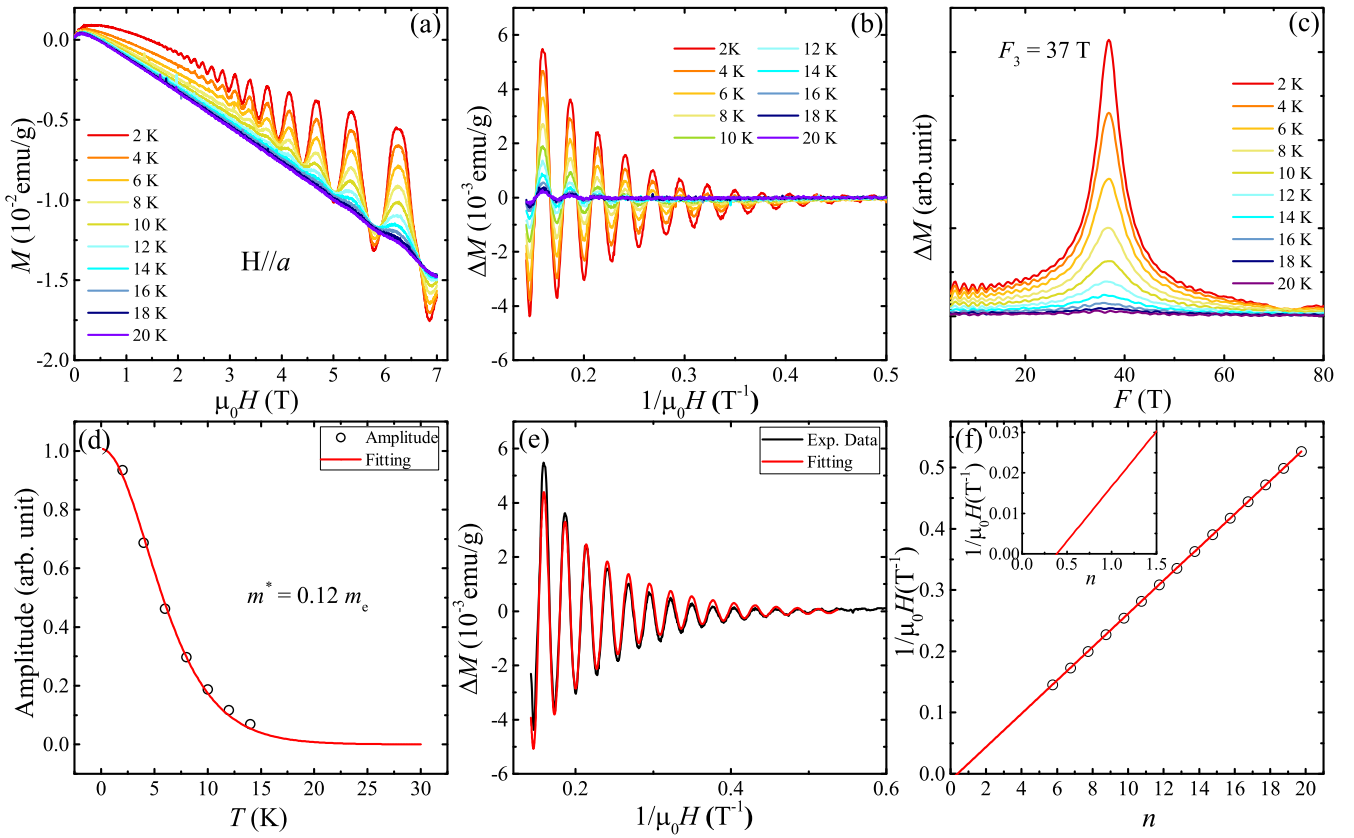


FIG. 5. The dHvA oscillations and nontrivial Berry phase. (a) Isothermal magnetization under $\mathbf{H} \parallel a$ at different temperatures starting from 2 K to 20 K. (b) The magnetization oscillations at different temperatures after subtracting the background. (c) The corresponding FFT spectrum. (d) The FFT amplitude as a function of temperature and the fit to R_T to determine the effective mass. (e) The Lifshitz-Kosevich fit (red line) of the oscillation pattern (black line) at 2 K. (f) The Landau fan diagram for the identified frequency. The inset enlarges the intersection.

for the electronic states in TaPdTe₅ [61]. Thus, the fitting parameters obtained from different methods consistently verify the nontrivial Berry phase in TaPdTe₅.

To further identify the topological electronic properties, we performed the full-potential linearized augmented plane wave method implemented in the WIEN2k package [42] for the electronic structure calculations, taking account of the SOC. The GGA presented by Wu and Cohen [43] was used for the exchange-correlation energy calculations. The calculated band structure is shown in Fig. 6(a), with five bands crossing the Fermi level. Similarly to the quasi-one-dimensional Tl₂Mo₆Se₆ compound [62,63], TaPdTe₅ also possesses cubic Dirac crossings, which have linear band crossings along one principle axis but the cubic dispersions in the plane perpendicular to it. The red arrows indicate the cubic Dirac crossings at high-symmetry points: $Z(0, 0, 0.5)$ and $T(-0.5, 0.5, 0.5)$, and the blue arrow indicates the standard linear Dirac crossing at $Y(-0.5, 0.5, 0)$. \mathbb{Z}_2 topological indices ($\nu_0; \nu_1\nu_2\nu_3$) are usually used in the classification of topological band insulators and semimetals [64]. Therefore, we have calculated the \mathbb{Z}_2 topological number, which is valid for time-reversal-invariant systems. A tight-binding model based on Wannier functions [44,45] was constructed to obtain the topological properties, using Ta d , Pd d , and Te p orbitals with SOC included. The \mathbb{Z}_2 topological number for 3D bulk systems can be obtained from the calculation of the Wilson loop for the six

time-reversal-invariant momentum planes. The \mathbb{Z}_2 invariants of TaPdTe₅ are 1 for the $k_x = \pi/a$, $k_y = \pi/b$, $k_z = 0$ plane, while zero for other planes. The topological index is (1; 110), which indicates that TaPdTe₅ is a topological nontrivial material. From the surface state spectrum in Fig. 6(b), there is a surface Dirac cone at the $\bar{\Gamma}$ point, which is also characteristic of a strong topological material [23]. More detailed results and discussions of first-principles calculations will be given elsewhere in a separate paper.

IV. SUMMARY

In summary, we have successfully synthesized the high-quality single crystal of a new layered ternary telluride TaPdTe₅ with quasi-1D PdTe₂ chains. Hall resistivity measurement indicates the coexistence of highly mobile but unbalanced electron and hole carriers. Anisotropic MR behaviors are found for magnetic fields and currents applied along different crystallographic axes. The MR for $\mathbf{I} \parallel a$ and $\mathbf{H} \parallel b$ can be separated into a linear term in addition to a conventional component, expected for Dirac fermions and conventional carriers, respectively, while the MR for $\mathbf{I} \parallel c$ and $\mathbf{H} \parallel b$ up to 51.7 T exhibits a power-law dependence even in high-field range. The anomalous nonsaturating high MR of $\sim 10^4\%$ at 2.1 K and 51.7 T for $\mathbf{I} \parallel c$ possibly bears the relation to unconventional quasiparticles in TaPdTe₅. SdH

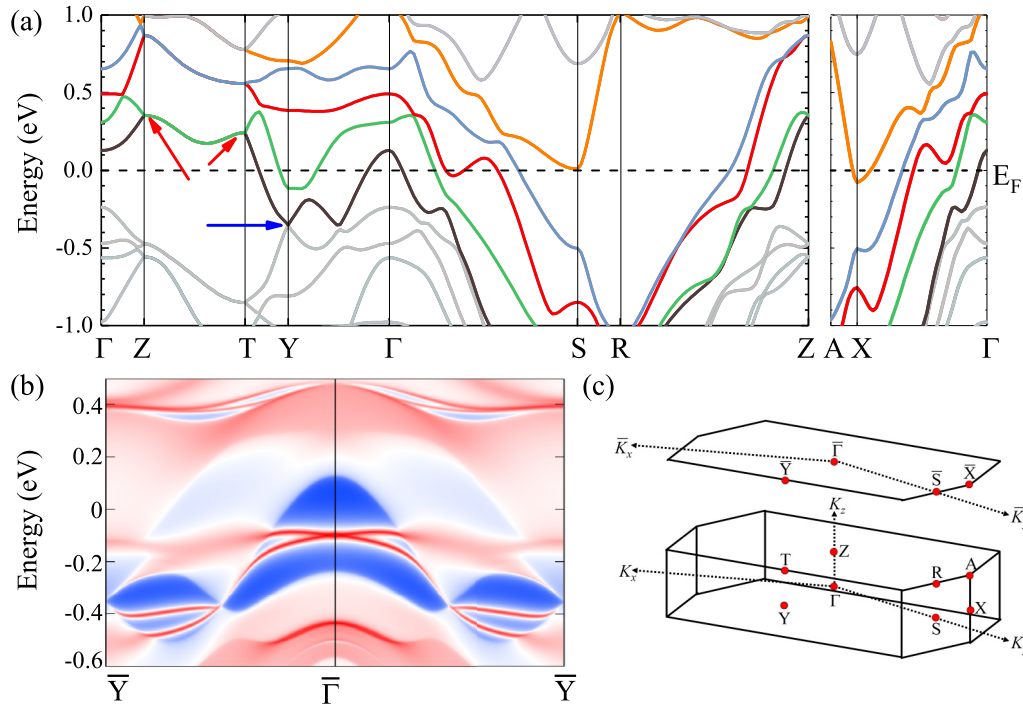


FIG. 6. (a) Calculated band structure for TaPdTe₅ with spin-orbit coupling included. The bands crossing the Fermi level are marked by different colors. The red and blue arrows indicate the positions of Dirac points. (b) Surface state spectrum of TaPdTe₅. (c) The bulk Brillouin zone (BZ) and (001) surface BZ of TaPdTe₅ with high-symmetry points marked in red.

oscillations under high magnetic fields give the light effective masses of charge carriers. More interestingly, clear dHvA oscillations reveal a nontrivial Berry phase in TaPdTe₅. The first-principles calculations indeed verify that TaPdTe₅ is a topological nontrivial material and possesses ordinary Dirac crossing as well as cubic Dirac crossing. As we have demonstrated in the initial trial, its atomically thin layers can be easily obtained through mechanical exfoliation. Therefore, the new layered telluride TaPdTe₅ provides a new platform to study the nontrivial physics belonging to “relativistic” carriers in low dimensions. Angle-dependent dHvA oscillations and angle-resolved photoemission spectroscopy are urgently called for to provide further insights into its Fermiology and the topological nature and identify the contributing pocket of each frequency. In the future, it would be also intriguing to explore the possible topological superconductivity in TaPdTe₅ by chemical substitution, intercalation, or high pressure.

ACKNOWLEDGMENTS

The authors would like to thank J. K. Bao for his constructive suggestions on the single-crystal diffraction experiment. Thanks are also due to S. Y. Li for fruitful discussions. This work was supported by Zhejiang Provincial Natural Science Foundation of China (No. LY19A040002). X.F.X. would like to acknowledge financial support from the National Natural Science Foundation of China (Grants No. 11974061 and No. U1732162). B.L. was supported by the National Natural Science Foundation of China (Grant No. 11674054) and NUPTSF (Grants No. NY220038 and No. NY219087). G.-H.C. acknowledges support from the National Key Research and Development Program of China (Grants No. 2017YFA0303002 and No. 2016YFA0300202). Z.-W.Z. acknowledges financial support from the National Key Research and Development Program of China (Grant No. 2016YFA0401704).

- [1] M. Z. Hasan and C. L. Kane, Colloquium: Topological insulators, *Rev. Mod. Phys.* **82**, 3045 (2010).
- [2] X. L. Qi and S. C. Zhang, Topological insulators and superconductors, *Rev. Mod. Phys.* **83**, 1057 (2011).
- [3] X. Wan, A. M. Turner, A. Vishwanath, and S. Y. Savrasov, Topological semimetal and Fermi-arc surface states in the electronic structure of pyrochlore iridates, *Phys. Rev. B* **83**, 205101 (2011).
- [4] Z. Wang, Y. Sun, X. Qiu Chen, C. Franchini, G. Xu, H. Weng, X. Dai, and Z. Fang, Dirac semimetal and topological phase

transitions in A₃Bi (A = Na, K, Rb), *Phys. Rev. B* **85**, 195320 (2012).

- [5] Z. K. Liu, B. Zhou, Y. Zhang, Z. J. Wang, H. M. Weng, D. Prabhakaran, S. K. Mo, Z. X. Shen, Z. Fang, X. Dai, Z. Hussain, and Y. L. Chen, Discovery of a three-dimensional topological Dirac semimetal Na₃Bi, *Science* **343**, 864 (2014).
- [6] Z. K. Liu, J. Jiang, B. Zhou, Z. J. Wang, Y. Zhang, H. M. Weng, D. Prabhakaran, S. K. Mo, H. Peng, P. Dudin, T. Kim, M. Hoesch, Z. Fang, X. Dai, Z. X. Shen, D. L. Feng, Z. Hussain,

- and Y. L. Chen, A stable three-dimensional topological Dirac semimetal Cd_3As_2 , *Nat. Mater.* **13**, 677 (2014).
- [7] H. Weng, C. Fang, Z. Fang, B. A. Bernevig, and X. Dai, Weyl Semimetal Phase in Noncentrosymmetric Transition-Metal Monophosphides, *Phys. Rev. X* **5**, 011029 (2015).
- [8] Z. K. Liu, L. X. Yang, Y. Sun, T. Zhang, H. Peng, H. F. Yang, C. Chen, Y. Zhang, Y. F. Guo, D. Prabhakaran, M. Schmidt, Z. Hussain, S. K. Mo, C. Felser, B. Yan, and Y. L. Chen, Evolution of the Fermi surface of Weyl semimetals in the transition metal pnictide family, *Nat. Mater.* **15**, 27 (2016).
- [9] S. Y. Xu, I. Belopolski, N. Alidoust *et al.*, Discovery of a Weyl Fermion semimetal and topological Fermi arcs, *Science* **349**, 613 (2015).
- [10] S. M. Huang, S. Y. Xu, I. Belopolski, C. C. Lee, G. Chang, B. Wang, N. Alidoust, G. Bian, M. Neupane, C. Zhang, S. Jia, A. Bansil, H. Lin, and M. Z. Hasan, A Weyl fermion semimetal with surface Fermi arcs in the transition metal monopnictide TaAs class, *Nat. Commun.* **6**, 7373 (2015).
- [11] H. J. Noh, J. Jeong, E. J. Cho, K. Kim, B. I. Min, and B. G. Park, Experimental Realization of Type-II Dirac Fermions in a PdTe_2 Superconductor, *Phys. Rev. Lett.* **119**, 016401 (2017).
- [12] F. C. Fei, X. Y. Bo, R. Wang, B. Wu, J. Jiang, D. Z. Fu, M. Gao, H. Zheng, Y. L. Chen, X. F. Wang, H. J. Bu, F. Q. Song, X. G. Wan, B. G. Wang, and G. H. Wang, Nontrivial Berry phase and type-II Dirac transport in the layered material PdTe_2 , *Phys. Rev. B* **96**, 041201(R) (2017).
- [13] A. A. Soluyanov, D. Gresch, Z. Wang, Q. Wu, M. Troyer, X. Dai, and B. A. Bernevig, Type-II Weyl semimetals, *Nature (London)* **527**, 495 (2015).
- [14] G. Bian, T. R. Chang, R. Sankar *et al.*, Topological nodal-line fermions in spin-orbit metal PbTaSe_2 , *Nat. Commun.* **7**, 10556 (2016).
- [15] J. Hu, Z. J. Tang, J. Y. Liu, X. Liu, Y. L. Zhu, D. Graf, K. Myhro, S. Tran, C. N. Lau, J. Wei, and Z. Q. Mao, Evidence of Topological Nodal-Line Fermions in ZrSiSe and ZrSiTe , *Phys. Rev. Lett.* **117**, 016602 (2016).
- [16] T. Liang, Q. Gibson, M. N. Ali, M. Liu, R. J. Cava, and N. P. Ong, Ultrahigh mobility and giant magnetoresistance in the Dirac semimetal Cd_3As_2 , *Nat. Mater.* **14**, 280 (2015).
- [17] Y. Zhao, H. Liu, C. Zhang *et al.*, Anisotropic Fermi Surface and Quantum Limit Transport in High Mobility Three-Dimensional Dirac Semimetal Cd_3As_2 , *Phys. Rev. X* **5**, 031037 (2015).
- [18] X. Huang, L. Zhao, Y. Long, P. Wang, D. Chen, Z. Yang, H. Liang, M. Xue, H. Weng, Z. Fang, X. Dai, and G. Chen, Open Access Observation of the Chiral-Anomaly-Induced Negative Magnetoresistance in 3D Weyl Semimetal TaAs, *Phys. Rev. X* **5**, 031023 (2015).
- [19] C. Zhang, C. Guo, H. Lu, X. Zhang, Z. Yuan, Z. Lin, J. Wang, and S. Jia, Large magnetoresistance over an extended temperature regime in monophosphides of tantalum and niobium, *Phys. Rev. B* **92**, 041203 (2015).
- [20] M. Alidoust, K. Halterman, and A. A. Zyuzin, Superconductivity in type-II Weyl semimetals, *Phys. Rev. B* **95**, 155124 (2017).
- [21] D. Li, B. Rosenstein, B. Y. Shapiro, and I. Shapiro, Effect of the type-I to type-II Weyl semimetal topological transition on superconductivity, *Phys. Rev. B* **95**, 094513 (2017).
- [22] T. E. O'Brien, M. Diez, and C. W. J. Beenakker, Magnetic Breakdown and Klein Tunneling in a Type-II Weyl Semimetal, *Phys. Rev. Lett.* **116**, 236401 (2016).
- [23] H. J. Zhang, C. X. Liu, X. L. Qi, X. Dai, Z. Fang, and S. C. Zhang, Topological insulators in Bi_2Se_3 , Bi_2Te_3 and Sb_2Te_3 with a single Dirac cone on the surface, *Nat. Phys.* **5**, 438 (2009).
- [24] Y. L. Chen, J. G. Analytis, J. H. Chu, Z. K. Liu, S. K. Mo, X. L. Qi, H. J. Zhang, D. H. Lu, X. Dai, Z. Fang, S. C. Zhang, I. R. Fisher, Z. Hussain, and Z. X. Shen, Experimental realization of a three-dimensional topological insulator, Bi_2Te_3 , *Science* **325**, 178 (2009).
- [25] M. N. Ali, J. Xiong, S. Flynn, J. Tao, Q. D. Gibson, L. M. Schoop, T. Liang, N. Haldolaarachchige, M. Hirschberger, N. P. Ong, and R. J. Cava, Large, nonsaturating magnetoresistance in WTe_2 , *Nature (London)* **514**, 205 (2014).
- [26] D. Rhodes, R. Schönemann, N. Aryal, Q. Zhou, Q. R. Zhang, E. Kampert, Y. C. Chiu, Y. Lai, Y. Shimura, G. T. McCandless, J. Y. Chan, D. W. Paley, J. Lee, A. D. Finke, J. P. C. Ruff, S. Das, E. Manousakis, and L. Balicas, Bulk Fermi surface of the Weyl type-II semimetallic candidate γ - MoTe_2 , *Phys. Rev. B* **96**, 165134 (2017).
- [27] Y. Liu, J. Z. Zhao, L. Yu, C. T. Lin, A. J. Liang, C. Hu, Y. Ding, Y. Xu, S. L. He, L. Zhao, G. D. Liu, X. L. Dong, J. Zhang, C. T. Chen, Z. Y. Xu, H. M. Weng, X. Dai, Z. Fang, and X. J. Zhou, Identification of topological surface state in PdTe_2 superconductor by angle-resolved photoemission spectroscopy, *Chin. Phys. Lett.* **32**, 067303 (2015).
- [28] M. Yan, H. Huang, K. Zhang, E. Wang, W. Yao, K. Deng, G. H. Wan, H. Zhang, M. Arita, H. Yang, Z. Sun, H. Yao, Y. Wu, S. Fan, W. Duan, and S. Zhou, Lorentz-violating type-II Dirac fermions in transition metal dichalcogenide PtTe_2 , *Nat. Commun.* **8**, 257 (2017).
- [29] C. Q. Xu, B. Li, W. H. Jiao, W. Zhou, B. Qian, R. Sankar, N. D. Zhigadlo, Y. Qi, D. Qian, F. C. Chou, and X. Xu, Topological type-II Dirac fermions approaching the Fermi level in a transition metal dichalcogenide NiTe_2 , *Chem. Mater.* **30**, 4823 (2018).
- [30] K. Koepf, D. Kasinathan, D. V. Efremov, S. Khim, S. Borisenko, B. Büchner, and J. van den Brink, TaIrTe_4 : A ternary type-II Weyl semimetal, *Phys. Rev. B* **93**, 201101(R) (2016).
- [31] J. W. Liu, H. Wang, C. Fang, L. Fu, and X. F. Qian, van der Waals stacking-induced topological phase transition in layered ternary transition metal chalcogenides, *Nano Lett.* **17**, 467 (2017).
- [32] Seunghyun Khim, K. Koepf, D. V. Efremov, J. Klotz, T. Förster, J. Wosnitza, M. I. Sturza, S. Wurmehl, C. Hess, J. van den Brink, and B. Büchner, Magnetotransport and de Haas-van Alphen measurements in the type-II Weyl semimetal TaIrTe_4 , *Phys. Rev. B* **94**, 165145 (2016).
- [33] R. Schönemann, Y. C. Chiu, W. K. Zheng, V. L. Quito, S. Sur, G. T. McCandless, J. Y. Chan, and L. Balicas, Bulk Fermi surface of the Weyl type-II semimetallic candidate NbIrTe_4 , *Phys. Rev. B* **99**, 195128 (2019).
- [34] W. Zhou, B. Li, C. Q. Xu, M. R. van Delft, Y. G. Chen, X. C. Fan, B. Qian, Nigel E. Hussey, and X. F. Xu, Nonsaturating magnetoresistance and nontrivial band topology of type-II Weyl semimetal NbIrTe_4 , *Adv. Electron. Mater.* **5**, 1900250 (2019).
- [35] Y. Xing, Z. B. Shao, J. Ge, J. W. Luo, J. H. Wang, Z. W. Zhu, J. Liu, Y. Wang, Z. Y. Zhao, J. Q. Yan, D. Mandrus, B. H. Yan, X. J. Liu, M. H. Pan, and J. Wang, Surface superconductivity in the type-II Weyl semimetal TaIrTe_4 , *Natl. Sci. Rev.* **7**, 579 (2020).

- [36] W. H. Jiao, Z. T. Tang, Y. L. Sun, Y. Liu, Q. Tao, C. M. Feng, Y. W. Zeng, Z. A. Xu, and G. H. Cao, Superconductivity in a layered $\text{Ta}_4\text{Pd}_3\text{Te}_{16}$ with PdTe_2 chains, *J. Am. Chem. Soc.* **136**, 1284 (2014).
- [37] W. H. Jiao, L. P. He, Y. Liu, X. F. Xu, Y. K. Li, C. H. Zhang, N. Zhou, Z. A. Xu, S. Y. Li, and G. H. Cao, Superconductivity in $\text{Ta}_3\text{Pd}_3\text{Te}_{14}$ with quasi-one-dimensional PdTe_2 chains, *Sci. Rep.* **6**, 21628 (2016).
- [38] G. Autès, A. Isaeva, L. Moreschini, J. C. Johannsen, A. Pisoni, R. Mori, W. T. Zhang, T. G. Filatova, A. N. Kuznetsov, L. Forró, W. Broek, Y. Kim, K. S. Kim, A. Lanzara, J. D. Denlinger, E. Rotenberg, A. Bostwick, M. Grioni, and O. V. Yazyev, A novel quasi-one-dimensional topological insulator in bismuth iodide $\beta\text{-Bi}_4\text{I}_4$, *Nat. Mater.* **15**, 154 (2016).
- [39] E. W. Liimatta and J. A. Ibers, Synthesis, structures, and conductivities of the new layered compounds $\text{Ta}_3\text{Pd}_3\text{Te}_{14}$ and TaNiTe_5 , *J. Solid State Chem.* **78**, 7 (1989).
- [40] G. M. Sheldrick, A short history of SHELX, *Acta Cryst. A* **64**, 112 (2008).
- [41] See Supplemental Material at <http://link.aps.org/supplemental/10.1103/PhysRevB.102.075141> for details on the independent atomic sites, thermal displacement parameters, related bond lengths, and bond angles of TaPdTe_5 .
- [42] K. Schwarz, P. Blaha, and G. K. H. Madsen, Electronic structure calculations of solids using the WIEN2k package for material sciences, *Comput. Phys. Commun.* **147**, 71 (2002).
- [43] Z. Wu and R. E. Cohen, More accurate generalized gradient approximation for solids, *Phys. Rev. B* **73**, 235116 (2006).
- [44] A. A. Mostofi, J. R. Yates, G. Pizzi, Y.-S. Lee, I. Souza, D. Vanderbilt and N. Marzari, An updated version of wannier90: A tool for obtaining maximally-localised Wannier functions, *Comput. Phys. Commun.* **185**, 2309 (2014).
- [45] Q. S. Wu, S. N. Zhang, H. F. Song, M. Troyer, and A. A. Soluyanov, WannierTools: An open-source software package for novel topological materials, *Comput. Phys. Commun.* **224**, 405 (2018).
- [46] E. W. Liimatta and J. A. Ibers, Synthesis, structure, and physical properties of the new layered ternary chalcogenide NbNiTe_5 , *J. Solid State Chem.* **71**, 384 (1987).
- [47] A. Mar and J. A. Ibers, Synthesis, structure, and physical properties of the new layered ternary telluride TaPtTe_5 , *J. Solid State Chem.* **92**, 352 (1991).
- [48] E. W. Liimatta and J. A. Ibers, Synthesis, structure, and conductivity of the new ternary chalcogenide NbPdTe_5 , *J. Solid State Chem.* **77**, 141 (1988).
- [49] W. H. Jiao, Y. N. Huang, X. F. Xu, Y. K. Li, Y. Liu, Z. C. Wang, X. L. Xu, Y. X. Feng, C. M. Feng, and G. H. Cao, Normal-state properties of the quasi-one-dimensional superconductor $\text{Ta}_4\text{Pd}_3\text{Te}_{16}$, *J. Phys.: Condens. Matter* **31**, 325601 (2019).
- [50] G. A. Bain and J. F. Berry, Diamagnetic corrections and Pascal's constants, *J. Chem. Educ.* **85**, 532 (2008).
- [51] K. G. Wilson, The renormalization group: Critical phenomena and the Kondo problem, *Rev. Mod. Phys.* **47**, 773 (1975).
- [52] A. B. Pippard, *Magnetoresistance in Metals* (Cambridge University Press, Cambridge, 1989).
- [53] C. Q. Xu, W. Zhou, R. Sankar, X. Z. Xing, Z. X. Shi, Z. D. Han, B. Qian, J. H. Wang, Zengwei Zhu, J. L. Zhang, A. F. Bangura, N. E. Hussey, and Xiaofeng Xu, Enhanced electron correlations in the binary stannide PdSn_4 : A homologue of the Dirac nodal arc semimetal PtSn_4 , *Phys. Rev. Mater.* **1**, 064201 (2017).
- [54] K. Wang and C. Petrovic, Multiband effects and possible Dirac states in LaAgSb_2 , *Phys. Rev. B* **86**, 155213 (2012).
- [55] O. Pavlosiuk, P. Swatek, and P. Wiśniewski, Giant magnetoresistance, three-dimensional Fermi surface and origin of resistivity plateau in YSb semimetal, *Sci. Rep.* **6**, 38691 (2016).
- [56] Y. K. Li, L. Li, J. L. Wang, T. T. Wang, X. F. Xu, C. Y. Xi, C. Cao, and J. H. Dai, Resistivity plateau and negative magnetoresistance in the topological semimetal TaSb_2 , *Phys. Rev. B* **94**, 121115(R) (2016).
- [57] Y. L. Wang, L. R. Thoutam, Z. L. Xiao, J. Hu, S. Das, Z. Q. Mao, J. Wei, R. Divan, A. Luican-Mayer, G. W. Crabtree, and W. K. Kwok, Origin of the turn-on temperature behavior in WTe_2 , *Phys. Rev. B* **92**, 180402 (2015).
- [58] M. N. Ali, L. M. Schoop, C. Garg, J. M. Lippmann, E. Lara, B. Lotsch, and S. S. P. Parkin, Butterfly magnetoresistance, quasi-2D Dirac Fermi surface and topological phase transition in ZrSiS , *Sci. Adv.* **2**, e1601742 (2016).
- [59] D. Shoenberg, *Magnetic Oscillations in Metals* (Cambridge University Press, Cambridge, 1984).
- [60] G. P. Mikitik and Y. V. Sharlai, Manifestation of Berry's Phase in Metal Physics, *Phys. Rev. Lett.* **82**, 2147 (1999).
- [61] J. Xiong, Y. K. Luo, Y. H. Khoo, S. Jia, R. J. Cava, and N. P. Ong, High-field Shubnikov-de Haas oscillations in the topological insulator $\text{Bi}_2\text{Te}_2\text{Se}$, *Phys. Rev. B* **86**, 045314 (2012).
- [62] Z. Song, B. Li, C. Xu, S. Wu, B. Qian, T. Chen, P. K. Biswas, X. Xu, and J. Sun, Pressure engineering of the Dirac fermions in quasi-one-dimensional $\text{Tl}_2\text{Mo}_6\text{Se}_6$, *J. Phys.: Condens. Matter* **32**, 215402 (2020).
- [63] Q. H. Liu and A. Zunger, Predicted Realization of Cubic Dirac Fermion in Quasi-One-Dimensional Transition-Metal Monochalcogenides, *Phys. Rev. X* **7**, 021019 (2017).
- [64] L. Fu and C. L. Kane, Topological insulators with inversion symmetry, *Phys. Rev. B* **76**, 045302 (2007).